Available online at www.sciencedirect.com
SCIENCE DIRECT®
Journal of Computational Physics 209 (2005) 643–664
JOURNAL OF COMPUTATIONAL PHYSICS
www.elsevier.com/locate/jcp

Lanczos pseudospectral method for initial-value problems in electrodynamics and its applications to ionic crystal gratings

Andrei G. Borisov [a,b], Sergei V. Shabanov [b,c,*]

[a] *Laboratoire des Collisions Atomiques et Moléculaires, UMR CNRS-Université Paris-Sud 8625, Bât. 351, Université Paris-Sud, 91405 Orsay CEDEX, France*
[b] *Donostia International Physics Center (DIPC), P. Manuel de Lardizabal 4, 20018 San Sebastián, Spain*
[c] *Department of Mathematics, University of Florida, Gainesville, FL 32611, USA*

Received 9 August 2004; received in revised form 19 January 2005; accepted 26 March 2005
Available online 4 June 2005

Abstract

Maxwell's equations are cast in the form of the Schrödinger equation. The Lanczos propagation method is used in combination with the fast Fourier pseudospectral method to solve the initial-value problem. As a result, a time-domain, unconditionally stable, and highly efficient numerical algorithm is obtained for propagation and scattering of broad-band electromagnetic pulses in dispersive and absorptive media. As compared to conventional finite-difference time-domain methods, an important advantage of the proposed algorithm is a dynamical control of accuracy: Variable time steps or variable computational costs per time step with error control are possible. The method is illustrated with numerical simulations of extraordinary transmission and reflection in metal, dielectric, and ionic crystal gratings with rectangular and cylindrical geometry. The effects of polaritonic excitations on transmission (reflection) properties of ionic crystal gratings in the infra-red range are investigated in detail. In particular, it is shown that, in addition to structural (geometric) resonances, resonant polaritonic excitations can drastically change light transmission.

Keywords: Lanczos algorithm; Arnoldi process; Maxwell's equations; Time-domain algorithms; Pseudospectral methods; Gratings; Polaritonic excitations

1. Introduction

Recent developments in photonics and nanostructure materials [1,2] have increased interest in efficient and accurate algorithms for numerical simulations of propagation and scattering of short (broad band)

* Corresponding author.
E-mail addresses: borisov@lcam.u-psud.fr (A.G. Borisov), shabanov@phys.ufl.edu (S.V. Shabanov).

0021-9991/$ - see front matter © 2005 Elsevier Inc. All rights reserved.
doi:10.1016/j.jcp.2005.03.034

laser pulses in generic passive (dispersive and absorptive) media. Time-domain approaches for solving the Maxwell's equations might be more suitable for this purpose than frequency domain methods because the sought-for information, e.g. the scattering matrix, can be obtained within any desired frequency range by a single propagation. Coupled with laser ellipsometry of broad-band pulses, fast simulations of expected resonance patterns in the scattering amplitude appear to be an efficient tool to control quality of manufactured photonic devices. Unconditionally stable algorithms are especially advantageous for such tasks because of their applicability to simulate the electromagnetic wave propagation in practically all materials and target geometries without any assessment of admissible values of the system parameters. Another attractive property of time-domain methods is their universality. The very same algorithms can be used to calculate static properties of the system (e.g. a band structure of photonic crystals), and to simulate the electromagnetic pulse propagation in non-linear materials as well as in media with time-dependent properties.

The advantages of time-domain methods have been recognized for a long time in quantum mechanics where they are extensively used in the fields of chemical reaction dynamics [3], laser–matter interactions [4], etc. Highly efficient and accurate tools have been developed for the wave packet propagation and analysis of the results [3,5–9]. Since Maxwell's equations can be cast in the form of the Schrödinger equation, it is then natural to extend time-domain methods of quantum mechanics to numerical electrodynamics. Some realizations of this idea are rooted in the path integral representation of quantum theory (the Lie–Trotter product formula [10] or the split operator method [5,11,12]). Other methods exploit polynomial approximations of the fundamental solution of the Schödinger equation. For instance, the Chebychev time-propagation technique has been recently used to simulate the electromagnetic pulse propagation in *non-absorbing* media [13,14].

Here, it is proposed to use the Lanczos [15] and Lanczos–Arnoldi [16] methods for solving linear systems (for a review see, e.g. [17]) to obtain an unconditionally stable, time-domain solver of Maxwell's equations for passive media. The method enables a dynamical control of accuracy, meaning that computational costs are constantly optimized in the course of simulations with error control. In brief, the approach can be summarized as follows. Maxwell's equations are written in the form of the Schrödinger equation which is then solved by the Lanczos propagation scheme [18,5] (Section 2). The difference with the well studied quantum mechanical case is that the wave function is a multi-dimensional vector field and the Hamiltonian is non-Hermitian for absorbing media. The split operator method [5,11,12] and the Lanczos–Arnoldi method [16] have been used to include attenuation into the Lanczos propagation scheme, while preserving its unconditional stability (Section 4). Section 3 contains examples of the Hamiltonian formalism for passive medium models that are used in our numerical simulations.

The accuracy of the method is investigated in Section 5. In Section 6, the Lanczos propagation scheme is applied to study the scattering of broad-band electromagnetic pulses on various gratings. In particular, a resonant extraordinary reflection is observed for a periodic array of parallel cylinders made of non-dispersive dielectric. This effect is similar to the Wood anomalies [19] and related to the existence of trapped (quasi-stationary) electromagnetic modes supported by the grating geometry (guided wave resonances) [20]. Simulations of the scattering of broad-band pulses on metallic grating and grooves, whose dielectric properties are described by the Drude model, are performed to demonstrate that the Lanczos propagation scheme is able to reproduce the results known in the literature and obtained by different means (by finite differences schemes or by the scattering matrix method).

We also study a grating structure consisting of parallel ionic crystal cylinders periodically arranged in vacuum. From the numerical point of view, the model of the dielectric permeability of such a material is rather representative and used in a vast number of applications. From the physical point of view, the interest in gratings and photonic crystals made of this kind of material is due to two types of effects in interaction with electromagnetic radiation: The structural and polaritonic ones [21,22]. We show that in the infra-red range, the reflection and transmission properties of ionic crystal gratings change significantly in narrow frequency ranges due to structural and polaritonic resonances. Structural resonances are associated with the existence

of trapped modes. Polaritonic resonances appear when the incident radiation can cause polaritonic excitations in the medium. From the macroscopic point of view, this occurs in the anomalous dispersion region of the dielectric constant.

2. The Lanczos method for Maxwell's equations

Let $\mathbf{D}$ and $\mathbf{B}$ be electric and magnetic inductions, respectively, and $\mathbf{E}$ and $\mathbf{H}$ the corresponding fields. When no external currents and charges are present, the dynamical Maxwell's equations read

$$\dot{\mathbf{D}} = c\nabla \times \mathbf{H}, \quad \dot{\mathbf{B}} = -c\nabla \times \mathbf{E}. \tag{2.1}$$

The over-dot denotes the time derivative, and c is the speed of light in the vacuum. Eq. (2.1) have to be supplemented by the Gauss law $\nabla \cdot \mathbf{D} = 0$ and also by $\nabla \cdot \mathbf{B} = 0$. Relations between the fields and inductions are determined by the medium in question. We begin with the case of a non-dispersive medium. Dispersive media are considered in Section 3. The medium response to the applied field is local in time, $\mathbf{D} = \varepsilon\mathbf{E}$ and $\mathbf{B} = \mu\mathbf{H}$ where ε and μ are positive, symmetric, position dependent matrices for generic non-isotropic and non-homogeneous media. For isotropic media, ε and μ are scalars. Maxwell's equations are rewritten in the form of the Schrödinger equation

$$\mathrm{i}\dot{\psi} = \mathscr{H}\psi, \quad \psi = \begin{pmatrix} \mathbf{E} \\ \mathbf{H} \end{pmatrix}, \quad \mathscr{H} = \begin{pmatrix} 0 & \mathrm{i}c\varepsilon^{-1}\nabla\times \\ -\mathrm{i}c\mu^{-1}\nabla\times & 0 \end{pmatrix}. \tag{2.2}$$

One can also use the electromagnetic inductions as independent variables instead of the fields. The Hamiltonian $\mathscr{H}$ must then be modified accordingly. The initial-value problem is solved by applying the evolution operator (or the fundamental solution) to the initial wave function

$$\psi(t) = \mathrm{e}^{-\mathrm{i}\mathscr{H}t}\psi(0). \tag{2.3}$$

At interfaces of different media, the boundary conditions are enforced dynamically, that is, ε and μ are allowed to have discontinuities. This is similar to quantum mechanical systems with discontinuous potentials (e.g. a well, a barrier, etc.). The Hamiltonian is a Hermitian operator, $\mathscr{H}^\dagger = \mathscr{H}$, with respect to the measure scalar product

$$(\psi_1, \psi_2) = \int (\mathbf{D}_1 \cdot \mathbf{E}_2 + \mathbf{B}_1 \cdot \mathbf{H}_2)\, \mathrm{d}\mathbf{r} \equiv \int \psi_1^\dagger \kappa \psi_2 \, \mathrm{d}\mathbf{r}. \tag{2.4}$$

The symmetric positive matrix κ is block-diagonal, with the blocks being ε and μ. The norm of the wave function with respect to the scalar product (2.4) is proportional to the electromagnetic energy and is conserved because the evolution operator is unitary.

Here, we adopt a pseudospectral approach to solving numerically our master equation (2.2). The Hilbert space is orthogonally projected onto a finite dimensional subspace by means of a suitable basis. In our simulations, we use the Fourier basis associated with a uniform periodic spatial grid [23]. In the grid representation, the wave function ψ becomes a vector whose components are values of ψ at grid sites, and the Hamiltonian $\mathscr{H}$ is a matrix. If the Hamiltonian is Hermitian, it is then convenient to have $\mathscr{H}$ as an explicitly Hermitian matrix. In the Maxwell theory, this can be achieved if, before projecting onto the grid, the wave function and the Hamiltonian are scaled

$$\psi \to \kappa^{-1/2}\psi, \quad \mathscr{H} \to \kappa^{-1/2}\mathscr{H}\kappa^{1/2}. \tag{2.5}$$

In the representation (2.2), we have

$$\mathbf{E} \to \varepsilon^{-1/2}\mathbf{E},\ \mathbf{H} \to \mu^{-1/2}\mathbf{H}, \quad \mathscr{H} \to \begin{pmatrix} 0 & \mathrm{i}c\varepsilon^{-1/2}\nabla \times \mu^{-1/2} \\ -\mathrm{i}c\mu^{-1/2}\nabla \times \varepsilon^{-1/2} & 0 \end{pmatrix}. \tag{2.6}$$

The scaled Hamiltonian is Hermitian with respect to the conventional scalar product in the space of square integrable functions, and, hence, it is a Hermitian matrix, when projected onto the grid by means of the Fourier-grid pseudospectral method.

It should be noted that, even though we use the Fourier-grid pseudospectral method in our numerical simulations, its choice is not special for the time-propagation scheme being developed, and motivated by its well-known virtues such as high accuracy in approximating spatial derivatives and exponential convergence [24]. As a point of fact, any discretization (projection) scheme suitable to compute the action of the Hamiltonian on the wave function in numerical simulations, e.g. finite differencing, finite elements, etc., can be used on equal footing with pseudospectral methods. Our study is focused on approximations of the fundamental solution of the Schrödinger equation in (2.3), i.e., on time propagation for a given choice of a finite-dimensional projection of $\mathscr{H}$.

A direct use of (2.3) implies a diagonalization of $\mathscr{H}$, which is not feasible if the matrix size is too large. Various numerical approximations are based on the semigroup property of the evolution operator

$$\psi(t+\Delta t) = \mathrm{e}^{-\mathrm{i}\Delta t\mathscr{H}}\psi(t). \tag{2.7}$$

The infinitesimal evolution operator can be approximated by a polynomial for a sufficiently small time step Δt. The basic idea of the Lanczos propagation method is that the exact solution $\psi(t+\Delta t)$ is projected onto the Krylov subspace associated with the initial state $\psi(t)$ and the Hamiltonian $\mathscr{H}$, $\psi(t+\Delta t) \to \psi^{(n)}(t+\Delta t) \equiv \mathscr{P}_n\psi(t+\Delta t) \in \mathsf{K}_n$, where $\mathscr{P}_n^\dagger = \mathscr{P}_n, \mathscr{P}_n^2 = \mathscr{P}_n$, and

$$\mathsf{K}_n = \mathrm{Span}(\psi(t), \mathscr{H}\psi(t), \ldots, \mathscr{H}^{n-1}\psi(t)).$$

The accuracy of such an approximation is $\mathrm{O}(\Delta t^n)$. The Hamiltonian is projected accordingly, $\mathscr{H} \to \mathscr{H}^{(n)} \equiv \mathscr{P}_n\mathscr{H}\mathscr{P}_n$. Thus,

$$\psi(t+\Delta t) \approx \psi^{(n)}(t+\Delta t) = \mathrm{e}^{-\mathrm{i}\Delta t\mathscr{H}^{(n)}}\psi^{(n)}(t) \equiv \mathscr{G}_{(n)}(\Delta t)\psi^{(n)}(t). \tag{2.8}$$

The matrix $\mathscr{G}_{(n)}(\Delta t)$ is called the amplification matrix. The projection is done via an orthonormal basis for K_n which is constructed by means of the Lanczos recursion algorithm [15]. In this basis, the matrix $\mathscr{H}^{(n)}$ is Hermitian and tridiagonal. Typically, just a few orders are sufficient ($n \leqslant 9$) so that n is much smaller than the dimension of $\mathscr{H}$ and the matrix $\mathscr{H}^{(n)}$ can easily be diagonalized. The dimension n may be set differently at each time step, depending on the current vector $\psi(t)$, and is determined by a pre-set required accuracy. In particular, it enables to avoid excessive actions of $\mathscr{H}$ on the wave function. This feature leads to a dynamical optimization of computational costs with error control, which is one the greatest advantages of the Lanczos method.

A detailed discussion of the Lanczos recursion algorithm and its application to the wave packet propagation can be found elsewhere [18,5]. Here, only a brief summary is given with notations used later in the text. Let $\psi_0 = \psi(t)$, where $\psi(t)$ is assumed to be normalized so that $\|\psi_0\| = 1$. Due to the linearity of the Schrödinger equation one can always scale ψ_0 by a number and rescale it back after applying the infinitesimal evolution operator. Define:

$$\alpha_0 = (\psi_0, \mathscr{H}\psi_0), \tag{2.9}$$

$$\phi_1 = (\mathscr{H} - \alpha_0)\psi_0, \tag{2.10}$$

$$\psi_1 = \phi_1/\|\phi_1\|. \tag{2.11}$$

By construction, ψ_1 and ψ_0 are orthonormal. For $k = 2,3,\ldots,n-1$, the rest of the basis for K_n is generated by the recursion relation:

$$\alpha_{k-1} = (\psi_{k-1}, \mathscr{H}\psi_{k-1}), \tag{2.12}$$

$$\beta_{k-2} = (\psi_{k-2}, \mathscr{H}\psi_{k-1}), \tag{2.13}$$

$$\phi_k = (\mathscr{H} - \alpha_{k-1})\psi_{k-1} - \beta_{k-2}\psi_{k-2}, \tag{2.14}$$

$$\psi_k = \phi_k/\|\phi_k\|. \tag{2.15}$$

By construction, the vector $\mathscr{H}\psi_j$ is a linear combination of ψ_{j-1}, ψ_j, and ψ_{j+1}. Hence, in the Lanczos basis the matrix $\mathscr{H}^{(n)}_{ij} = (\psi_i, \mathscr{H}\psi_j)$ is tridiagonal. Elementary calculations show that the diagonal elements are $\mathscr{H}^{(n)}_{jj} = \alpha_j = \bar{\alpha}_j$, the upper and lower superdiagonals are $\mathscr{H}^{(n)}_{jj+1} = \mathscr{H}^{(n)}_{j-1j} = \beta_j = \bar{\beta}_j$.

Let U be a unitary transformation such that $U^\dagger \mathscr{H}^{(n)} U$ is a diagonal matrix and $E^{(n)}_j$ be the eigenvalues of $\mathscr{H}^{(n)}$. The approximate solution (2.8) is obtained by expanding the wave function over the Lanczos basis and solving the Schödinger equation for the expansion coefficients

$$\psi^{(n)}(t + \Delta t) = \sum_{k,j=0}^{n-1} \bar{U}_{jk} \mathrm{e}^{-\mathrm{i}\Delta t E^{(n)}_j} U_{j0}\psi_k \equiv \sum_{k=0}^{n-1} c_k(\Delta t)\psi_k, \tag{2.16}$$

where the initial condition $c_k(0) = \delta_{k0}$ has been taken into account. Since $\mathscr{H}^{(n)}$ is Hermitian, the evolution preserves the norm

$$\|\psi^{(n)}(t + \Delta t)\|^2 = \|\psi^{(n)}(t)\|^2 = \|\psi_0\|^2 = 1. \tag{2.17}$$

Recall that a time-stepping algorithm is unconditionally stable if the norm of all powers of its amplification matrix are uniformly bounded, that is, $\|\mathscr{G}^N_{(n)}\| \leqslant \text{const}$ uniformly for all integers $N > 0$, $\Delta t > 0$, and all other parameters of $\mathscr{G}_{(n)}$ [25]. The norm of the amplification matrix is defined by $\|\mathscr{G}_{(n)}\| = \sup_\psi \|\mathscr{G}_{(n)}\psi\|/\|\psi\|$. It follows from (2.17) that the algorithm is unconditionally stable because $\|\mathscr{G}^N_{(n)}\| \leqslant \|\mathscr{G}_{(n)}\|^N = 1$.

The accuracy of the algorithm can be estimated from the following observation [18]. The norm of an orthogonal projection of the exact solution onto the orthogonal complement of K_n can be used as a measure of accuracy of the Lanczos algorithm. By expanding the exponential in the right hand side of (2.7) into a Taylor series, it is clear that the contribution of the term $(\Delta t\mathscr{H})^{n+1}\psi(t)$, which has no projection onto K_n, can only be captured by the approximate solution if the larger Krylov space K_{n+2} is used in the Lanczos algorithm, which, in turn, implies that the vector $c_j(\Delta t)$ acquires two additional components. Thus, the accuracy of the Lanczos algorithm can be controlled, for example, by demanding that the absolute value of $c_{n-1}(\Delta t)$ is less than a specified small number ϵ. Note that $|c_{n-1}(\Delta t)| \sim \mathrm{O}(\Delta t^{n-1})$ as one can deduce from (2.16), the tridiagonal structure of $\mathscr{H}^{(n)}$ in the Lanzcos basis, and the initial condition $c_k(0) = \delta_{k0}$. To ensure that the norm of the projection of $\psi(t + \Delta t)$ onto the orthogonal complement of K_n is small, we demand that

$$|c_{n-3}(\Delta t)|^2 + |c_{n-2}(\Delta t)|^2 + |c_{n-1}(\Delta t)|^2 \leqslant \epsilon, \tag{2.18}$$

where $\epsilon \sim 10^{-14}$ in our calculations. To satisfy (2.18), the time step Δt, or the dimension of the Krylov subspace n, or both can be varied to minimize computational costs. This is the aforementioned dynamical control of accuracy in the Lanczos propagation method. In our simulations, Δt has been kept fixed, while (2.18) has been used to determine a minimal n for each time step. Some care should be taken regarding a known drawback of the Lanczos algorithm – a possible loss of orthogonality of basis functions due to round-off errors [15,26]. This is why in all the examples presented in this paper the time step has been adjusted so that only low dimensional Krylov spaces, $n \leqslant 9$, are invoked in contrast to the conventional use of the Lanczos method for solving linear systems.

3. Examples of media with attenuation

In the case of generic passive media, relations between the inductions and fields in (2.1) are no longer local in time. However, the medium response to the applied electromagnetic field must be causal. A common way to model the causal response is to assume that the medium polarization, $\mathbf{P} = \mathbf{D} - \mathbf{E}$, and magnetization $\mathbf{M} = \mathbf{B} - \mathbf{H}$, satisfy linear differential equations in time in which a non-homogeneous term is proportional to the applied field (for linear media). The Maxwell's equations in passive media appear then to be a system of (high-order) differential equations to which numerical algorithms are applied [27,28]. Any system of high-order differential equations can be converted into a system of first-order differential equations by introducing auxiliary dynamical variables. This idea is used to convert Maxwell's equations for passive media into the Schrödinger equation (2.2) in which the wave function contains additional components that describe dynamics of the medium polarization and magnetization [12].

Due to absorption the time evolution is no longer unitary. From the mathematical point of view, the Hamiltonian acquires an imaginary part, $\mathscr{H} = \mathscr{H}_0 - \mathrm{i}\mathscr{V}$ where $\mathscr{H}_0^\dagger = \mathscr{H}_0$ and $\mathscr{V}^\dagger = \mathscr{V}$. The system is absorbing and, therefore, $\mathscr{V}$ must be a positive semidefinite operator, that is, for any $\psi, (\psi, \mathscr{V}\psi) \geqslant 0$. This readily follows from the condition that the norm of a solution of (2.2) cannot increase with time. The Lanczos method should be modified to incorporate this new feature, while retaining its key virtues such as unconditional stability and dynamical accuracy control. Before we do so, let us illustrate the formal mathematical concept of attenuation with specific examples of media later used in our numerical simulations.

It must also be noted that an additional, artificial absorption of the wave packet is required in numerical simulations of scattering problems in which the pulse shape is to be computed in the asymptotic region. Indeed, when the front edge of the pulse reaches the grid boundary, it will be reflected or re-appear on the other side of the grid, depending on the boundary conditions. To avoid an artificial interference of the scattered pulse with itself, a layer of an absorbing medium is necessary at the grid boundary [29].

3.1. The Drude model of metals

In the Drude model, the magnetization $\mathbf{M} = 0$, while the dielectric constant ε is a function of the frequency ω given by

$$\varepsilon(\omega) = 1 - \frac{\omega_\mathrm{p}^2}{\omega^2 + \mathrm{i}\eta\omega}, \tag{3.1}$$

where $\eta > 0$ is the attenuation constant and ω_p is the plasma frequency, which is set to zero in vacuum and to some specific value in the metal (see Section 6). The corresponding medium polarization obeys the second order differential equation

$$\ddot{\mathbf{P}} + \eta\dot{\mathbf{P}} = \omega_\mathrm{p}^2\mathbf{E}, \tag{3.2}$$

subject to vanishing initial conditions, $\mathbf{P}(0) = \dot{\mathbf{P}}(0) = 0$. Define an auxiliary field $\mathbf{Q}$ by $\dot{\mathbf{P}} = \omega_\mathrm{p}\mathbf{Q}$. Rewriting the Maxwell's equations and (3.2) in terms $\mathbf{E}$, $\mathbf{B}$, and $\mathbf{Q}$ and their first-order time derivatives, the Schrödinger equation is obtained in which

$$\psi = \begin{pmatrix} \mathbf{E} \\ \mathbf{B} \\ \mathbf{Q} \end{pmatrix}, \quad \mathscr{H} = \begin{pmatrix} 0 & \mathrm{i}c\boldsymbol{\nabla}\times & -\mathrm{i}\omega_\mathrm{p} \\ -\mathrm{i}c\boldsymbol{\nabla}\times & 0 & 0 \\ \mathrm{i}\omega_\mathrm{p} & 0 & -\mathrm{i}\eta \end{pmatrix}. \tag{3.3}$$

The Hamiltonian is Hermitian when $\eta = 0$ (no attenuation). The attenuation potential $\mathscr{V}$ is a diagonal matrix, $\mathrm{diag}(0,0,\eta)$, that is positive semidefinite since $\eta > 0$.

3.2. Ionic crystal materials

Dielectric properties of ionic crystal materials are well described by a dielectric constant given as a function of the frequency ω by

$$\varepsilon(\omega) = \varepsilon_\infty + \frac{(\varepsilon_0 - \varepsilon_\infty)\omega_\mathrm{T}^2}{\omega_\mathrm{T}^2 - \omega^2 - \mathrm{i}\eta\omega}, \tag{3.4}$$

where $\varepsilon_{\infty,0}$ are constants, ω_T is the resonant frequency, and η is the attenuation. Let $\mathbf{P}$ be the dispersive part of the total polarization vector of the medium. Then $\mathbf{D} = \varepsilon_\infty\mathbf{E} + \mathbf{P}$. By using the Fourier transform, it is straightforward to deduce that $\mathbf{P}$ satisfies the second-order differential equation

$$\ddot{\mathbf{P}} + \eta\dot{\mathbf{P}} + \omega_\mathrm{T}^2\mathbf{P} = \varepsilon_\infty\omega_\mathrm{p}^2\mathbf{E}, \tag{3.5}$$

where $\omega_\mathrm{p}^2 = (\varepsilon_0 - \varepsilon_\infty)\omega_\mathrm{T}^2/\varepsilon_\infty$ if $\varepsilon_0 - \varepsilon_\infty$ is positive, otherwise, $\omega_\mathrm{p}^2 \to -\omega_\mathrm{p}^2$ in (3.5). Eq. (3.5) must be solved with zero initial conditions, $\mathbf{P} = \dot{\mathbf{P}} = 0$ at $t = 0$.

Define a set of auxiliary fields $\mathbf{Q}_{1,2}$ by $\mathbf{P} = \sqrt{\varepsilon_\infty}\omega_\mathrm{p}\mathbf{Q}_1/\omega_\mathrm{T}$ and $\dot{\mathbf{Q}}_1 = \omega_\mathrm{T}\mathbf{Q}_2$. For non-magnetic media ($\mu = 1$), Maxwell's equations and (3.5) can be written as a Schrödinger equation in which the wave function and the Hamiltonian are defined by

$$\psi = \begin{pmatrix} \varepsilon_\infty^{1/2}\mathbf{E} \\ \mathbf{B} \\ \mathbf{Q}_1 \\ \mathbf{Q}_2 \end{pmatrix}, \quad \mathscr{H} = \begin{pmatrix} 0 & \mathrm{i}c\varepsilon_\infty^{-1/2}\mathbf{\nabla}\times & 0 & -\mathrm{i}\omega_\mathrm{p} \\ -\mathrm{i}c\mathbf{\nabla}\times\varepsilon_\infty^{-1/2} & 0 & 0 & 0 \\ 0 & 0 & 0 & \mathrm{i}\omega_\mathrm{T} \\ \mathrm{i}\omega_\mathrm{p} & 0 & -\mathrm{i}\omega_\mathrm{T} & -\mathrm{i}\eta \end{pmatrix}. \tag{3.6}$$

Here $\varepsilon_{\infty,0}$ are set to one in the vacuum and to some specific values in the medium in question (see Section 6). The squared norm of the wave function, $\|\psi\|^2 = \int \mathrm{d}\mathbf{r}\,\psi^\dagger\psi$, is proportional to the total electromagnetic energy of the wave packet [12,30]. When attenuation is not present, $\eta = 0$, the Hamiltonian is Hermitian, $\mathscr{H}^\dagger = \mathscr{H}$, and the norm (or energy) is conserved. As seen from (3.6) the attenuation potential is a diagonal matrix: $\mathscr{V} = \mathrm{diag}(0, 0, 0, \eta)$.

3.3. Absorbing boundary conditions

For the additional absorber at the grid boundaries, a layer of a conducting medium has been used with a position-dependent conductivity σ. The induced current in a conducting medium has the form $\mathbf{J} = \sigma\mathbf{E}$. If $\mathscr{V}_{11}$ is the element in the upper left corner of the attenuation potential $\mathscr{V}$, then it has to be changed to $\mathscr{V}_{11} - 4\pi\sigma$ to include the absorbing layer. The function $\sigma \geqslant 0$ is constructed according to the frequency band of the initial pulse (for details see [12,30] and references therein).

4. Including attenuation

4.1. The split method

A simple way to include the attenuation of the wave packet amplitude into the Lanczos method, while maintaining the unconditional stability of the algorithm, is to use the split operator method. The exact time evolution (2.7) is approximated by means of the Lie–Trotter formula

$$\psi(t + \Delta t) = \mathrm{e}^{-\Delta t\mathscr{V}/2}\mathrm{e}^{-\mathrm{i}\Delta t\mathscr{H}_0}\mathrm{e}^{-\Delta t\mathscr{V}/2}\psi(t) + \mathrm{O}(\Delta t^3) \equiv \mathscr{G}^{\mathrm{LS}}(\Delta t)\psi(t) + \mathrm{O}(\Delta t^3). \tag{4.1}$$

The action of the exponential of $\mathscr{H}_0$ is computed by the Lanczos method as before. The attenuation potential $\mathscr{V}$ typically does not involve spatial derivatives and, hence, the action of its exponential on a wave function is far less expensive than that for $\mathscr{H}_0$. The norm of any power of the amplification matrix $\mathscr{G}^{\mathrm{LS}}(\Delta t)$ still remains uniformly bounded by unity because $\|\mathrm{e}^{-\Delta t\mathscr{V}/2}\| \leqslant 1$ for $\Delta t \geqslant 0$. Hence, unconditional stability is preserved. A disadvantage is, however, that the dynamical accuracy control is lost because the accuracy is now mostly determined by the split (4.1) rather than by the dimension of the Krylov space associated with $\mathscr{H}_0$. This would not be a significant shortcoming of the scheme if the attenuation was only used to enforce absorbing boundary conditions because the accuracy of the numerical solution in the spatial region occupied by the absorbing layer is not important anyway (see Section 5.2).

4.2. The Lanczos–Arnoldi method

The dynamical accuracy control in systems with attenuation can be restored in several ways. One mathematically sound possibility is to use the dually orthonormal Lanczos basis in which $\mathscr{H}^{(n)}$ retains the tridiagonal complex symmetric structure [15]. In the special case of a complex symmetric $\mathscr{H}$, the use of the dual Krylov space can be avoided. There is an orthogonal Lanczos basis for K_n in which $\mathscr{H}^{(n)}$ is also complex symmetric tridiagonal, but orthogonality is now understood with respect to a new scalar product (without complex conjugation of vectors) [17]. However, in both cases, the "projector" $\mathscr{P}_n$ is no longer Hermitian. This has an unpleasant consequence. One can show that, while the accuracy remains of the order $\mathrm{O}(\Delta t^n)$, unconditional stability is typically lost. The algorithm is only conditionally stable. A more detailed study of such schemes will be given elsewhere.

It is possible to achieve unconditional stability and dynamical control of accuracy at the same time, but at the price of having an algorithm that is slightly less "memory friendly". It is based on the Arnoldi process for non-Hermitian matrices. Let us construct an orthonormal basis for K_n applying, for example, the Gramm–Schmidt process to linearly independent Krylov vectors. The projector $\mathscr{P}_n$ constructed in this basis is Hermitian. The difference with the conventional Lanczos scheme for Hermitian Hamiltonians is that the matrix $\mathscr{H}^{(n)}$ has a Hessenberg form, that is, it is upper-triangular with one extra non-zero lower superdiagonal [16,17]. Compared to the costs of computing consecutive actions of $\mathscr{H}$ on the wave function, a direct diagonalization of $\mathscr{H}^{(n)}$ is still inexpensive for small n.

The recurrence relation is similar to (2.14). Put $\phi_0 = \psi(t)$ and $\psi_0 = \phi_0/\|\phi_0\|$. Compute $\mathscr{H}^{(n)}_{00} = (\psi_0, \mathscr{H}\psi_0)$. For $j = 1,2,\ldots,n-1$, compute:

$$\phi_j = \mathscr{H}\psi_{j-1} - \sum_{k=0}^{j-1} \mathscr{H}^{(n)}_{kj-1}\psi_k, \tag{4.2}$$

$$\psi_j = \phi_j/\|\phi_j\|, \quad \mathscr{H}^{(n)}_{jj-1} = (\psi_j, \mathscr{H}\psi_{j-1}), \tag{4.3}$$

and, for $k = 0,1,\ldots,j$, compute

$$\mathscr{H}^{(n)}_{kj} = (\psi_k, \mathscr{H}\psi_j). \tag{4.4}$$

By construction, $(\psi_j,\psi_k) = \delta_{jk}$. A one-time-step evolution is again given by (2.16). Observe the key difference with the Lanczos scheme. In numerical simulations, the Lanczos recurrence relation (2.14) requires to store only two preceding basis vectors in the operational memory, while in (4.2) all the preceding basis vectors must be kept in the operational memory. Fortunately, in practice the dimension of the Krylov space is not large at any time step so that the increased demand for memory usage does not appear as a significant problem.

Now we prove that the algorithm is unconditionally stable. Observe that before the projection onto the Krylov space, the evolution operator is uniformly bounded $\|\exp(-\mathrm{i}\Delta t\mathscr{H})\| \leqslant 1$ for $\Delta t > 0$ and all param-

eters of $\mathscr{H}$ for which the attenuation operator $\mathscr{V}$ remains positive semidefinite. The amplification matrix has the form $\mathscr{G}_{(n)}(\Delta t) = \exp(-\mathrm{i}\Delta t\mathscr{H}^{(n)})$. Thanks to the Hermiticity of $\mathscr{P}_n$, it is sufficient to show that $\mathscr{V}^{(n)} = \mathscr{P}_n\mathscr{V}\mathscr{P}_n$ is positive semidefinite because the latter implies that $\|\mathscr{G}^N_{(n)}(\Delta t)\| \leqslant \|\mathscr{G}_{(n)}(\Delta t)\|^N \leqslant 1$ uniformly for all integers $N > 0$, $\Delta t > 0$, and all parameters of $\mathscr{H}$. For any ψ, the following chain of equalities holds, $(\psi, \mathscr{V}^{(n)}\psi) = (\psi, \mathscr{P}_n\mathscr{V}\mathscr{P}_n\psi) = (\psi^{(n)}, \mathscr{V}\psi^{(n)}) \geqslant 0$. In the first equality, the definition of $\mathscr{V}^{(n)}$ has been used, in the second one, the Hermiticity of the projection operator has been invoked, and the final inequality is valid since $\mathscr{V}$ is positive semidefinite. The proof is completed.

The same condition (2.18) can be used for the dynamical accuracy control. Recall that this condition is based on the fact that $c_{n-1}(\Delta t) \sim \mathrm{O}(\Delta t^{n-1})$ because c_{n-1} determines the weight of $\mathscr{H}^{n-1}\psi(t)$ in the Taylor expansion of $\psi^{(n)}(t + \Delta t)$. In the case of a non-Hermitian $\mathscr{H}$, the time evolution of the vector $\mathbf{c}$ is generated by a Hessenberg matrix $\mathscr{H}^{(n)}$. By examining the Taylor expansion of the exponential in $\exp(-\mathrm{i}\Delta t\mathscr{H}^{(n)})\mathbf{c}(0)$, it is easy to convince oneself that $c_{n-1}(\Delta t) \sim \mathrm{O}(\Delta t^{n-1})$ remains valid. Indeed, thanks to the Hessenberg form of the matrix $\mathscr{H}^{(n)}$, that is, $\mathscr{H}^{(n)}$ has only zeros below the lower superdiagonal, the action of $[\mathscr{H}^{(n)}]^k$ on the initial vector $c_j(0) = \delta_{j0}$ produces a vector with the first $k + 1$ non-zero entries. Hence, only for $k = n - 1$ a non-zero bottom entry appears in the vector $\mathbf{c}$.

5. Time-propagation accuracy analysis

5.1. Free space propagation. Phase and amplitude errors

To illustrate the efficiency of the Lanczos time-propagation method, we compare it with a widely adopted Second Order Finite Difference (SOD, or leapfrog) propagation method [5,28,31], using the simplest example of the electromagnetic pulse propagation in vacuum. The action of the Hamiltonian on wave functions in the Lanczos and leapfrog methods are done in the same way, that is, by the fast Fourier pseudospectral method on the same grid.

Consider a Gaussian wave packet linearly polarized along the y-axis and propagating along the z-axis. The amplitude of the fields at the initial time $t = 0$ is given by

$$E_y(z) = \mathrm{e}^{-z^2/D^2}\mathrm{e}^{\mathrm{i}k_0 z}, \quad H_x(z) = -E_y(z), \tag{5.1}$$

where $k_0 = 5.5/D$ and D determines the width of the wave packet. The carrier wave length $\lambda = 2\pi/k_0$ so that $D = 0.875\lambda$. We take $D = 1.75$ μm, or $\lambda = 2$ μm. The step of the grid is $\Delta z = 0.1D$. An exact solution directly follows from (5.1) $E_y(z,t) = E_y(z - ct)$. The wave packet propagates in the direction of positive z. With our settings the pulse duration is about 25 fs.

Numerical solutions are obtained by the Lanczos and leapfrog algorithms for the Schrödinger equation (2.2) in which $\varepsilon = \mu = 1$. Recall that the leapfrog propagation scheme is based on the third-order finite difference approximation of the time derivative

$$\psi(t + \Delta t) = \psi(t - \Delta t) - 2\mathrm{i}\Delta t\mathscr{H}\psi(t). \tag{5.2}$$

The scheme is conditionally stable, and the time step must be chosen accordingly, $\Delta t\|\mathscr{H}\| \leqslant 1$ for $\mathscr{H}^\dagger = \mathscr{H}$ (for the non-Hermitian case see the discussion in [30]). The simulated electric field is recorded by a detector placed at $z = z_{\mathrm{det}} = 18D$. Its phase and amplitude are compared with those of the exact solution. For a signal $E(t) = E_0(t)\mathrm{e}^{\mathrm{i}\varphi(t)}$, where $E_0(t) = |E(t)|$, the phase and amplitude errors are defined, respectively, by

$$\delta^P = \frac{|\varphi^{\mathrm{exact}} - \varphi^{\mathrm{approx}}|}{\varphi^{\mathrm{exact}}}, \quad \delta^A = \frac{|E_0^{\mathrm{exact}} - E_0^{\mathrm{approx}}|}{E_0^{\mathrm{exact}}}. \tag{5.3}$$

The errors $\delta^{P,A}$ are plotted, respectively, in Figs. 1 and 2 as functions of $S = (z_{\mathrm{det}} - ct)/D$, the position of the pulse center relative to the detector measured in units of D. The results are shown for $|S| \leqslant 2.5$, where the

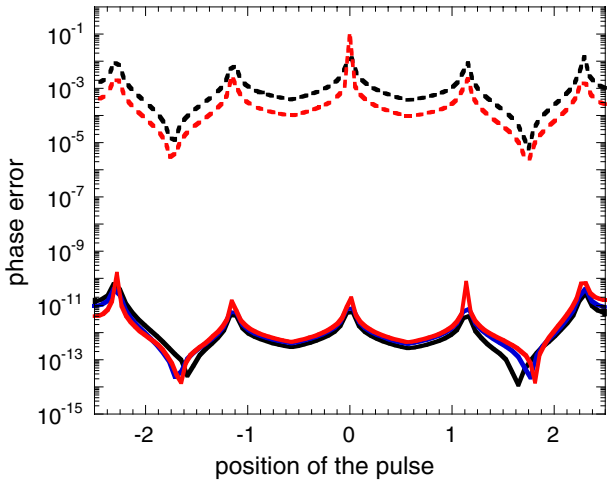

Fig. 1. Phase errors for the propagation of an electromagnetic Gaussian pulse in vacuum. Results are presented as a function of the position of the pulse center relative to the detector, S, measured in units of the pulse width D. Dashed and solid curves correspond, respectively, to the leapfrog and Lanczos propagation methods. Different colors represent computational costs of simulations measured as the total number of actions of the Hamiltonian on the wave function for fixed propagation time. Further details are given in the text. (For interpretation of the references to color in this figure legend, the reader is referred to the web version of this article.)

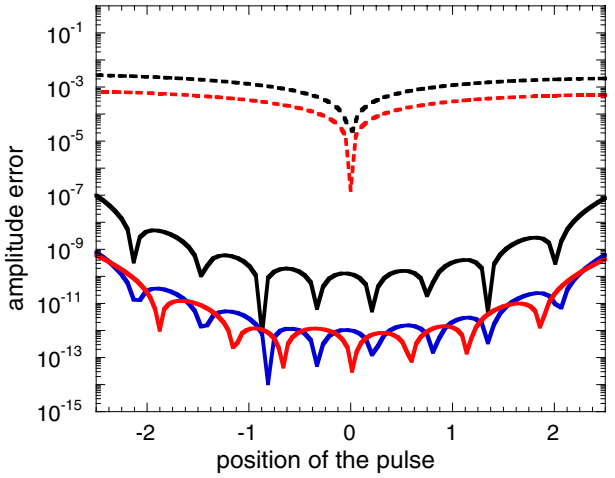

Fig. 2. Amplitude errors for the propagation of an electromagnetic Gaussian pulse in vacuum. Results are presented as a function of the position of the pulse center relative to the detector, S, measured in units of the pulse width D. Dashed and solid curves correspond, respectively, to the leapfrog and Lanczos propagation methods. Different colors represent computational costs of simulations measured as the total number of actions of the Hamiltonian on the wave function for fixed propagation time. Further details are given in the text. (For interpretation of the references to color in this figure legend, the reader is referred to the web version of this article.)

amplitude of the signal on the detector is sufficient. Time sampling points at the detector are chosen so that $\varphi^{\text{exact}}(t)$ does not vanish. Dashed and solid lines correspond to the leapfrog and Lanczos methods, respectively, for various settings of the time step.

The time step for the black dashed line is a reference time step, $\Delta t_0 \approx 0.01$ fs. If N_H is the number of elementary operations required to compute the action of the Hamiltonian on a wave function, then the total

number of operations reads $N = sN_H N_t$, where s is the number of actions of the Hamiltonian per a time step, $N_t = t/\Delta t$ is the total number of time steps. For the leapfrog method, $s = 1$ for all time steps. In the Lanczos method, $s = n - 1$, with n being the dimension of the Krylov space. Despite the fact that the dynamic control of accuracy has been activated, de facto n does not vary in the course of the simulations in vacuum.

Let $N = N_0$ for the black dashed curve. The red dashed curve is obtained by reducing the time step, $\Delta t = \Delta t_0/2$, and, hence, the total number of operations increases accordingly, $N = 2N_0$. In the Lanczos method, the black solid curve corresponds to $\Delta t = 10\Delta t_0$ and $s = 7$, the blue solid curve to $\Delta t = 5\Delta t_0$ and $s = 7$, and the red one to $\Delta t = 2.5\Delta t_0$ and $s = 6$. The total number of operations is, respectively, $N = 0.7N_0$, $N = 1.4N_0$, and $N = 2.4N_0$.

In summary, it is readily seen that at roughly the same number of operations, the Lanczos algorithm has phase and amplitude errors that are less than those in the leapfrog method by several orders of magnitude.

5.2. Comparison of different time-propagation schemes

There are, of course, algorithms that would be more efficient than the Lanczos propagation method in free space. For instance, the split propagation method [12] essentially reproduces an exact solution and is also unconditionally stable. However, the split method would not be applicable when the Hamiltonian involves products of operators that depend on spatial derivatives and positions. In general, the accuracy of a time stepping algorithm can be estimated by the deviation of the exact infinitesimal evolution operator from the amplification matrix in the operator norm

$$\delta(\Delta t) \equiv \|\mathrm{e}^{-\mathrm{i}\Delta t\mathscr{H}} - \mathscr{G}(\Delta t)\|. \tag{5.4}$$

Here, we discuss only the time-propagation accuracy, assuming that a required level of accuracy in the spatial dependence of the Hamiltonian has been achieved by a suitable method. In particular, accuracy and convergence of the Fourier-grid pseudospectral method used in our simulations can be found in [24]. In this sense, the exponential in (5.4) represents the exact evolution operator.

Now we compare the leapfrog (LF), Lanczos with the split (LS), and Lanczos–Arnoldi (LA) time-propagation schemes. There is an upper bound on error of Krylov subspace approximations to the matrix exponential operator [32], which, applied to our case of the Arnoldi process, yields

$$\delta^{\mathrm{LA}}(\Delta t) \leqslant 2(\Delta t\|\mathscr{H}\|)^n/n! \sim 2(\Delta t c k_{\max})^n/n!, \tag{5.5}$$

where $k_{\max}$ is the maximal wave vector supported by the spatial grid resolution. The bound can be significantly improved [33], by a factor $2^{-n}\exp(-p\Delta t\|\mathscr{H}\|)$ with $p > 0$ for $n \geqslant \Delta t\|\mathscr{H}\|$. This bound shows that the LA propagation scheme is superior to the LF method in both respects, the accuracy and convergence. While the LF scheme is only stable if $\Delta t c k_{\max} \leqslant 1$, the LA scheme enables larger time steps within the same required error tolerance. For some special non-Hermitian Hamiltonians, there is rapid error decay even for $n \gg \Delta t\|\mathscr{H}\|$ [33].

The accuracy of the LF scheme, $\delta^{\mathrm{LF}} \sim (\|\mathscr{H}\|\Delta t)^3 \sim (ck_{\max}\Delta t)^3$, can be improved by, for example, taking into account the next term of the Taylor expansion of ψ $(t \pm \Delta t)$ in powers of Δt in (5.2) [25,34] (which is similar to the so-called Lax–Wernoff method)

$$-2\mathrm{i}\Delta t\mathscr{H}\psi \to -2\mathrm{i}\Delta t\mathscr{H}(1 - \Delta t^2\mathscr{H}^2/3)\psi.$$

The method is still conditionally stable where the LF stability condition, $\Delta t\|\mathscr{H}\| \leqslant 1$, changes accordingly to $\Delta t\|\mathscr{H}(1 - \Delta t^2\mathscr{H}^2/3)\| \leqslant 1$. Even though s has tripled, the new stability condition allows one to increase the time step by the factor of 2.1. Therefore, the total number of operations increases only slightly. The accuracy of the scheme will be of order $(\|\mathscr{H}\|\Delta t)^5$, which is still not as high as in the LA method.

For not so large problems, the LS method might be more efficient than the LA method. Let N_0 be the total number grid points. If the Fourier pseudospectral method is used to compute the action of the Hamiltonian on wave function, then the number of operations required is $N_H = N_0 \log_2 N_0$ (based on the use of the fast Fourier algorithm). There are $s = n - 1$ actions of the Hamiltonian per time step in either algorithm. On the other hand, the number of operations required to compute matrix elements $\mathscr{H}^{(n)}_{jk}$ in the Lanczos and Arnoldi processes scales as $(2n - 1)N_0$ and $(n(n + 1)/2 + n - 1)N_0$, respectively. For large N_0 and small n, the costs of one time step in either algorithm is dominated by $sN_H = (n - 1)N_0 \log_2 N_0$. For not so large N_0, that is, when $\log_2 N_0 \sim n$, computing $\mathscr{H}^{(n)}_{jk}$ and the sums in the recurrence relation (4.2) becomes just as expensive as the actions of the Hamiltonian, while this is not so in the LS method because $\mathscr{H}^{(n)}_0$ has a tridiagonal symmetric structure in the Lanczos basis.

Even though the accuracy of the LS method is of order Δt^3, it is actually higher than the LF scheme accuracy. For some particular systems, the LS method might even be just as accurate as the LA scheme at the same or lower computational costs. This can be understood from the following observation. By making use of the Campbell–Hausdorf formula, we infer for the amplification matrix in the LS algorithm that

$$\mathrm{e}^{-\mathrm{i}\Delta t\mathscr{H}} - \mathscr{G}^{\mathrm{LS}}(\Delta t) = -\tfrac{1}{24}([\mathscr{H}_0, [\mathscr{H}_0, \mathscr{V}]] - 2\mathrm{i}[\mathscr{V}, [\mathscr{V}, \mathscr{H}_0]])\Delta t^3 + \mathrm{O}(\Delta t^4). \tag{5.6}$$

Taking, for example, the ionic crystal Hamiltonian (3.6), the commutators are straightforward to compute. Then the error introduced by the split is mostly determined by $\|[\mathscr{H}_0, [\mathscr{H}_0, \mathscr{V}]]\|\Delta t^3 \sim ck_{\max}\eta\Omega\Delta t^3$ and by $\|[\mathscr{V}, [\mathscr{V}, \mathscr{H}_0]]\|\Delta t^3 \sim \eta\Omega^2\Delta t^3$, where Ω stands for $\max(\omega_{\mathrm{p}}, \omega_{\mathrm{T}})$. Since $ck_{\max} \gg \Omega$ and $ck_{\max} \gg \eta$, the accuracy of the LS method appears to be higher than that of the LF scheme, $\delta^{\mathrm{LS}} \ll \delta^{\mathrm{LF}}$. The error of computing $\exp(-\mathrm{i}\Delta t\mathscr{H}_0)$ in the LS method is given again by (5.5) which is typically small compared to the error of the split approximation itself.

Depending on the parameters of the Hamiltonian, it is conceivable to get $\delta^{\mathrm{LS}} \sim \delta^{\mathrm{LA}}$ by reducing the time step in the LS method. Since the LA method could require more elementary operations per one time step, that is, when $\log_2 N_0 \sim n$, the LS method might happen to be more efficient, or, at least, be just as good as the LA method, that is, it would have the same accuracy at the lower or same computational costs. An absorbing layer is a good example of this.

6. Applications to nanostructured periodic materials

In this section, the Lanczos propagation scheme is applied to scattering of broad-band wave packets on nanostructured periodic materials such as gratings and grooves. We are particularly interested in transmission (reflection) properties, which are currently subjects of intense research [2,35–37]. The results obtained here are compared with those available in the literature. The time-dependent approach illuminates the significance of trapped modes or resonances for extraordinary transmittance and reflectance of periodic structures. The longer a trapped mode lives, the more narrow the resonance which occurs in the reflection and/or transmission coefficient.

All systems considered here have a translation symmetry along one of the Euclidean axes, chosen to be the y-axis. The structures are periodic along the x-axis with period D_{g}, while the z-direction is transverse to the structure. The initial-wave packet is Gaussian and propagates along the z-axis (see, e.g. (5.1)). Its spectrum is broad enough to cover the frequency range of interest. The frequency resolved transmission and reflection coefficients are obtained via the time-to-frequency Fourier transform of the signal on "virtual detectors" placed at some distance in front and behind the periodic structure [38]. The zero diffraction mode is studied here for wavelengths $\lambda \geqslant D_{\mathrm{g}}$ so that reflected and transmitted beams propagate along the z-axis. Similar to our previous work [30], we use a change of variables in both x ($x = f_1(\xi)$) and z ($z = f_2(\zeta)$) coordinates to enhance the sampling efficiency in the vicinity of medium interfaces so that the boundary

conditions are accurately reproduced by the Fourier-grid pseudospectral method. A typical size of the mesh corresponds to $-15D_g \leqslant z \leqslant 15D_g$, and $-0.5D_g \leqslant x \leqslant 0.5D_g$ with, respectively, 512 and 128 mesh points. Note that, because of the variable change, a uniform mesh in the auxiliary coordinates (ξ,ζ) corresponds to a non-uniform mesh in the physical (x,z) space.

6.1. Array of dielectric cylinders

The significance of trapped modes is first illustrated with a periodic array of non-dispersive dielectric cylinders, a system which has not received as much attention as metal or dielectric gratings with rectangular geometry. Consider an array of parallel, periodically positioned, dielectric cylinders in vacuum oriented along the y-axis. The packing density $R/D_g = 0.1$, where R is the radius of cylinders and $D_g = 1.75$ μm is the grating period. The incident wave packet is linearly polarized. The electric field is oriented along the y-axis, i.e., parallel to the cylinders (the so-called TE polarization). The Hamiltonian for the Lanczos scheme has the form (2.2) where $\mu = 1$.

In Fig. 3, the reflection coefficient $\mathscr{R}$ is shown as a function of the wave length expressed in units of D_g. In the Schrödinger formulation of Maxwell's theory, the squared norm of the wave function is proportional to the total electromagnetic energy. Hence, for a lossless medium the transmission $\mathscr{T}$ can simply be obtained from energy conservation: $\mathscr{T} + \mathscr{R} = 1$, since the Lanczos propagation method preserves the norm. The solid-blue and dashed-red curves correspond, respectively, to $\varepsilon = 2$ and $\varepsilon = 4$. As one can see the array becomes a perfect reflector within a fairly narrow wavelength range centered at the resonant wavelength, which is slightly larger than the period D_g. Similar results have been obtained for dielectric grating structures with rectangular geometry. The resonant pattern is associated with the so-called Wood anomalies [19], and can be explained by the existence of trapped modes or guided wave resonances [20,30]. The widths of the resonances in the reflection (transmission) coefficient are determined by the lifetime of a corresponding quasi-stationary trapped mode which is a standing wave along the x-axis and is excited by the incoming wave.

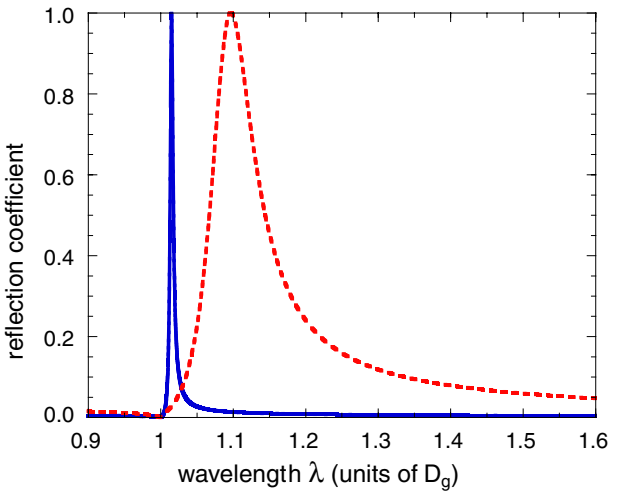

Fig. 3. Calculated zero-order reflection coefficient for a periodic array of dielectric cylinders in vacuum described in the text. Results are presented as a function of the wavelength of the incident radiation measured in units of the period D_g. The solid-blue and dashed-red curves correspond, respectively, to the array of cylinders with dielectric constants $\varepsilon = 2$ and $\varepsilon = 4$. (For interpretation of the references to color in this figure legend, the reader is referred to the web version of this article.)

The existence of trapped modes can easily be inferred from the temporal evolution of the electromagnetic field. Fig. 4 shows the transmitted electric field as a function of time measured by a detector placed behind the layer of dielectric cylinders. The main transmitted pulse is clearly visible. It has a significant amplitude and a duration about 25 fs. After the main pulse passes the array, it leaves behind an excited quasi-stationary mode which looses its energy by radiating an almost monochromatic wave. By symmetry, the same lasing effect is registered in the reflection direction by a detector placed in front of the layer (not shown here). The lasing effect of the trapped mode appears as exponentially damped oscillations coming after the main signal. An exponential decay due to a finite lifetime of the quasi-stationary state is clearly seen. A 100% reflection at the resonant frequency can be understood from the fact that the field emitted by the trapped mode in the transmission direction and the corresponding frequency component of the initially transmitted pulse have an opposite phase, thus, compensating each other. The solid-blue and dashed-red curves correspond, respectively, to $\varepsilon = 2$ and $\varepsilon = 4$. The radiation coming from the narrow resonance (the blue curve) has a lower amplitude and a much longer duration. The lifetime of the trapped mode in this case is in the picosecond range, i.e., a thousand times longer than the initial pulse duration. Note that the more narrow the resonance the less energy gets trapped from the initial pulse. This explains the amplitude difference of the blue and red curves. Finally, the concept of trapped modes localized on successive layers and interacting with each other provides a theoretical framework for light propagation in layered structures such as photonic crystal slabs [39].

6.2. Metal gratings and grooves

Metal gratings and grooves have been extensively studied in micro-wave and optical domains [35,36]. The purpose of this section is to show that the Lanczos-split propagation scheme (Section 4.1) can successfully be applied to metals described by the Drude model. The Hamiltonian has the form (3.3). For the sake of comparison with published results [35], the attenuation and the plasma frequency are taken to be: $\omega_p = 9$ eV and $\eta = 0.1$ eV. The grating geometry is sketched in the lower right corner of Fig. 5. The grating period $D_g = 1.75$ μm, the thickness (along the z-axis) $h = 0.8$ μm, and the grating width $a = 0.3$ μm. The

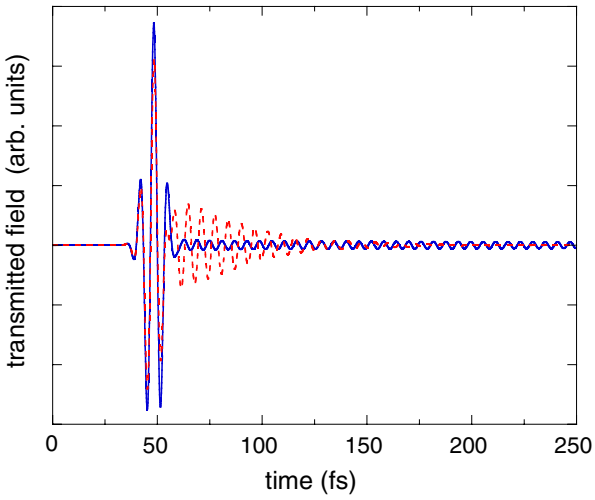

Fig. 4. Electric field measured by a detector placed behind the periodic layer of dielectric cylinders. Only the field corresponding to the zero-order transmitted wave propagating along the z-axis is represented. It is obtained by the Fourier analysis of the x-coordinate dependence of the field at the detector position. The signal is shown as a function of time measured in femtoseconds. The solid-blue and dashed-red curves correspond, respectively, to the array of cylinders with dielectric constants $\varepsilon = 2$ and $\varepsilon = 4$. (For interpretation of the references to color in this figure legend, the reader is referred to the web version of this article.)

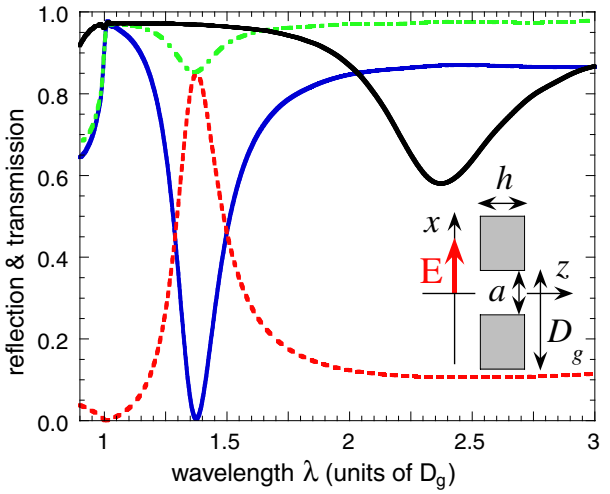

Fig. 5. Calculated zero-order reflection and transmission coefficients for metallic gratings and grooves described in the text. Results are presented as a function of the wavelength of the incident radiation measured in units of the period D_g. The inset in the lower right corner of the figure gives a schematic view on the grating geometry. The black line shows the reflection coefficient for metallic grooves. Blue and dashed-red line shows the reflection (transmission) coefficient for metallic gratings. The sum of the reflection and transmission coefficients for metallic gratings is shown as the dashed-dotted green curve. Its deviation from 1 represents the loss of electromagnetic energy because of the absorption in metal. (For interpretation of the references to color in this figure legend, the reader is referred to the web version of this article.)

corresponding grooves are obtained by attaching a solid metal plate on one side of the gratings so that no transmission is possible. The polarization of the incident wave packet is such that the electric field vector is oriented along the x-axis, i.e., perpendicular to the gratings (the so-called TM polarization). The difference with the non-dispersive case discussed above is the presence of attenuation. The trapped mode looses its energy due to imperfect conductivity of the metal. This leads to broadening of the resonance.

In Fig. 5, the dashed-red and solid-blue curves represent the transmission and reflection coefficients, respectively, as functions of the wavelength expressed in units of the grating period D_g. The resonance is again associated with the existence of a trapped stationary wave in the grating. The transmittance does not reach 100% due to a dissipative loss of energy in a Drude metal. While for a lossless medium the sum of the reflection and transmission coefficients must be one, this is not the case for the Drude metal (the dashed-dotted green curve in Fig. 5). The maximal loss of energy corresponds to the resonant wavelength. It is easily understood because the trapped mode remains in contact with the metal much longer than the main pulse, and, therefore, can dissipate more energy through exciting surface electrical currents in metal. The black curve in Fig. 5 shows the reflectance of the grooves. Since the light cannot be transmitted through the grooves, a resonance structure in the reflection coefficient is directly related to an enhanced energy loss at the wavelength of the trapped mode. Note that, as compared to the metal gratings, the resonance is broadened and shifted to the lower frequencies (larger wavelength). The results obtained here are in a full agreement with previous theoretical and numerical analysis [35,36].

6.3. Ionic crystal gratings

The Lanczos–Arnoldi algorithm (Section 4.2) has been applied to simulate the scattering of broad-band electromagnetic (laser) pulses on a grating structure consisting of circular parallel ionic crystal cylinders periodically arranged in vacuum. The Hamiltonian has the form (3.6). Our primary interest is to study the effect of trapped modes (guided wave resonances) and polaritonic excitations on the transmission

and reflection properties of the grating in the infra-red range. The dielectric function of the ionic crystal material is approximated by the single oscillator model (3.4). Following the work [21], we chose the parameters representative for the beryllium oxide: $\varepsilon_\infty = 2.99$, $\varepsilon_0 = 6.6$, $\omega_T = 87.0$ meV, and the damping $\eta = 11.51$ meV. The packing density, $R/D_g = 0.1$, has been kept fixed in simulations. The initial Gaussian wave packet is linearly polarized with the electric field oriented along the y-axis, i.e., parallel to the cylinders (the so-called TE polarization).

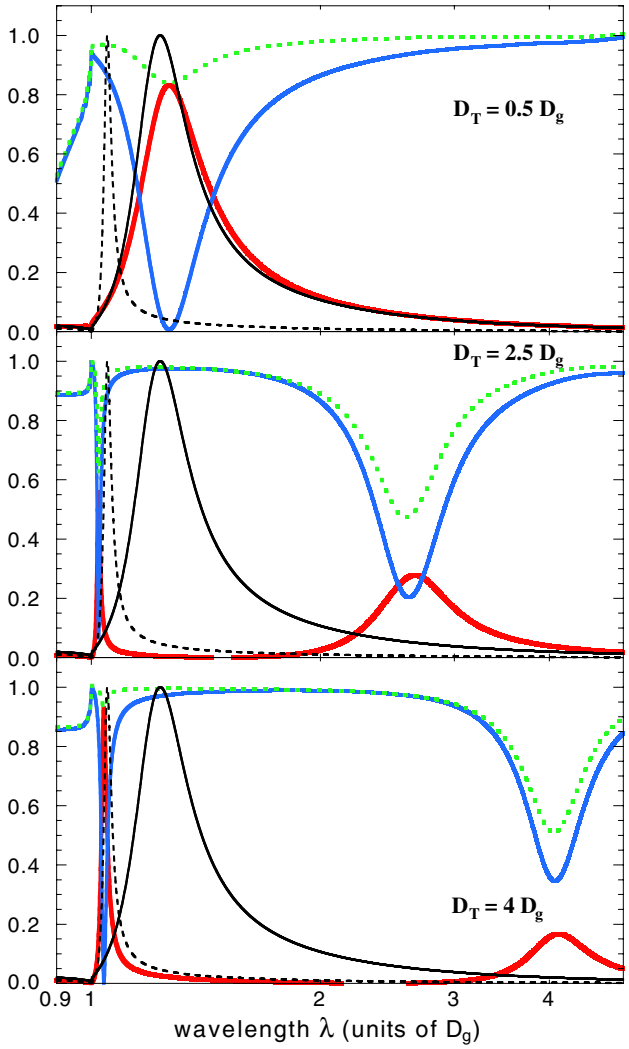

Fig. 6. Calculated zero-order reflection (red curves) and transmission (blue curves) coefficients for the ionic crystal grating described in the text. The results are presented as a function of the incident radiation wavelength measured in units of the grating period D_g. Different panels of the figure correspond to different values of the grating period as compared to the resonance wavelength, $D_T = 2\pi c/\omega_T$, for the polaritonic excitation of the material. The dashed and solid-black curves represent the reflection coefficient calculated for gratings made of a lossless, non-dispersive dielectric characterized by $\varepsilon = \varepsilon_\infty$ and $\varepsilon = \varepsilon_0$, respectively. The sum of the reflection and transmission coefficients is shown as the dashed-dotted green curve. Its deviation from 1 represents the electromagnetic energy loss because of attenuation. (For interpretation of the references to color in this figure legend, the reader is referred to the web version of this article.)

Two types of resonances are expected in the infra-red range for the gratings studied here. Structure resonances are characteristic for periodic dielectric gratings. They are associated with the existence of guided wave modes [20]. As demonstrated in the above example of non-dispersive dielectric grating (Section 6.1), in the absence of losses, structure resonances lead to 100% reflection within a narrow frequency interval(s) for wavelengths $\lambda \sim D_g$. The second type of resonances arise because of polaritonic excitations for wavelengths $\lambda \sim D_T = 2\pi c/\omega_T$. Calculations have been done for different values of D_g so that the polaritonic excitation can be tuned throughout the wavelength range of interest ($\lambda/D_g \geqslant 1$) by changing the ratio D_T/D_g.

In Fig. 6, we show the results obtained for the transmission (blue curves) and reflection (red curves) coefficients for the beryllium oxide gratings characterized by the period D_g such that $D_T/D_g = 0.5$, 2.5, and 4, as indicated in the figure. The results are presented as a function of the radiation wavelength measured in units of the grating period. Note that a logarithmic scale is used for the horizontal axis in order to improve the resolution at small wavelengths. Consider first the following two limiting cases. According to (3.4), for short wavelengths, $\lambda \ll D_T$ ($D_g \ll D_T$), the medium behaves as a dielectric with $\varepsilon \approx \varepsilon_\infty$. In the long wavelength limit $\lambda \gg D_T$ ($D_g \gg D_T$), the medium responds as a dielectric material characterized by $\varepsilon \approx \varepsilon_0$. In Fig. 6, the dashed and solid black curves represent the reflection coefficient of the grating made of lossless, non-dispersive dielectric cylinders with $\varepsilon = \varepsilon_\infty$ and $\varepsilon = \varepsilon_0$, respectively. In full agreement with results of Section 6.1 (Fig. 3), the reflection coefficient in these two cases reaches 1 within a narrow frequency range for $\lambda \sim D_g$. This resonant pattern is explained by the existence of guided wave resonances. The width of the

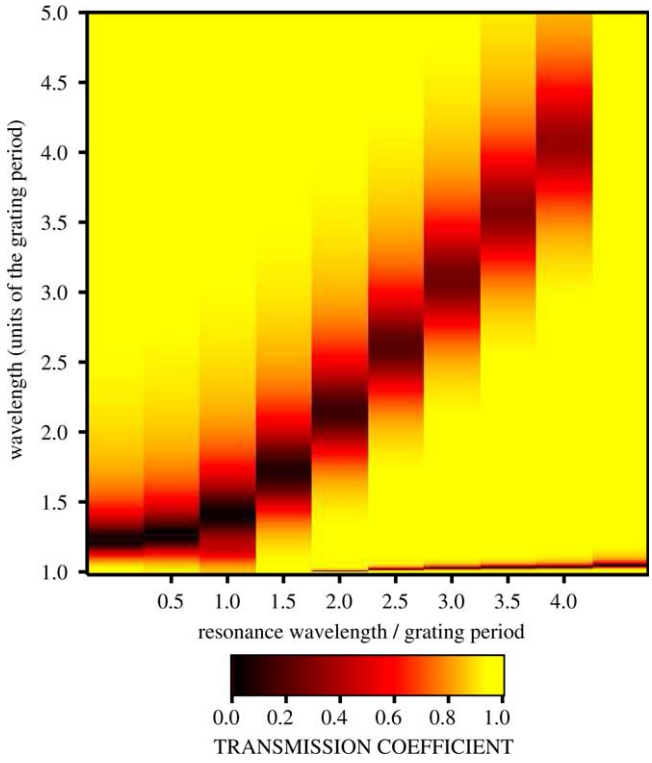

Fig. 7. Zero-order transmission coefficient for the ionic crystal grating described in the text as a function of the incident radiation wavelength and the grating period. The horizontal axis represents the ratio D_T/D_g of the resonance wavelength for the polaritonic excitation of the material $D_T = 2\pi c/\omega_T$ and the grating period D_g. The vertical axis represents the incident radiation wavelength λ measured in units of D_g. Color codes used for the plot are shown in the inset. (For interpretation of the references to color in this figure legend, the reader is referred to the web version of this article.)

resonances is determined by the lifetime of the corresponding quasi-stationary trapped mode, which is a standing wave along the x-axis and is excited by the incoming wave. The width increases with ε, while the resonant wavelength gets redshifted, which explains the difference between the dashed and solid black curves ($\varepsilon_0 > \varepsilon_\infty$).

Now we turn to a discussion of the effects due to dispersive properties of the ionic crystal material. For $D_T/D_g = 0.5$, the resonant excitation of polaritons is impossible within the range of wavelengths of interest, and the dielectric constant is close to ε_0. The result for the reflection coefficient in this case is similar to the data shown by the black solid curve. However, there is an essential difference as compared to the case of a lossless, non-dispersive dielectric grating. Indeed, the sum of the reflection and transmission coefficients (the dashed-dotted green curve) is not unity for the beryllium oxide model because of the damping. The same as in the case of the metal gratings and grooves (Fig. 5), the maximal loss of energy arises at the resonant wavelength.

For $D_T/D_g = 2.5$, two resonances emerge leading to the enhanced reflection within the corresponding frequency ranges. The one at $\lambda/D_g \sim 2.5$, i.e., $\lambda \sim D_T$, is associated with polaritonic excitations of the ionic crystal. The resonance at $\lambda \sim D_g$ is a structure resonance. As follows from (3.5), the dielectric constant in this case approaches ε_∞ for small wavelengths $\lambda \sim D_g$. Then the width and position of the structure resonance are close to the data given by the dashed black curve. The imaginary part of the dielectric function is

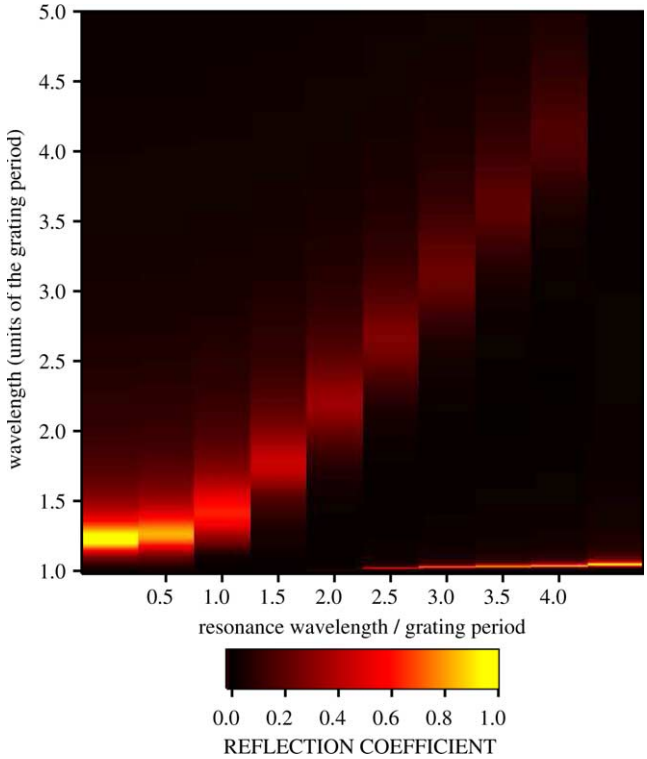

Fig. 8. Zero-order reflection coefficient for the ionic crystal grating described in the text as a function of the incident radiation wavelength and the grating period. The horizontal axis represents the ratio D_T/D_g of the resonance wavelength for the polaritonic excitation of the material $D_T = 2\pi c/\omega_T$ and the grating period D_g. The vertical axis represents the incident radiation wavelength λ measured in units of D_g. Color codes used for the plot are shown in the inset. (For interpretation of the references to color in this figure legend, the reader is referred to the web version of this article.)

large enough throughout the entire wavelength range to produce a substantial energy loss at both of the resonances.

Finally, for $D_T/D_g = 4$ the polaritonic excitation appears at $\lambda \sim 4D_g$ and the two resonances are well separated. The structure resonance at $\lambda \sim D_g$ closely matches the result for a lossless, non-dispersive dielectric grating characterized by $\varepsilon = \varepsilon_\infty$. Observe that the reflection coefficient is close to 1 in this case and the energy loss is small because the imaginary part of $\varepsilon(\omega)$ is small far from $\omega = \omega_T$.

Figs. 7 and 8 show, respectively, the transmission and reflection coefficients of the grating as functions of the incident radiation wavelength and the grating period D_g. The polariton resonance wavelength $D_T = 2\pi c/\omega_T$ and the packing density R/D_g are kept fixed. The results for the two limiting cases in which $\varepsilon = \varepsilon_0$ and $\varepsilon = \varepsilon_\infty$ are represented by the left-most and right-most colored columns, respectively. The resonance pattern of the system is clearly visible, and, in particular, the transformation of the structure resonance at $\varepsilon = \varepsilon_0$ into the polaritonic one. Thus, by increasing the ratio D_T/D_g, the "broad" structure resonance associated with

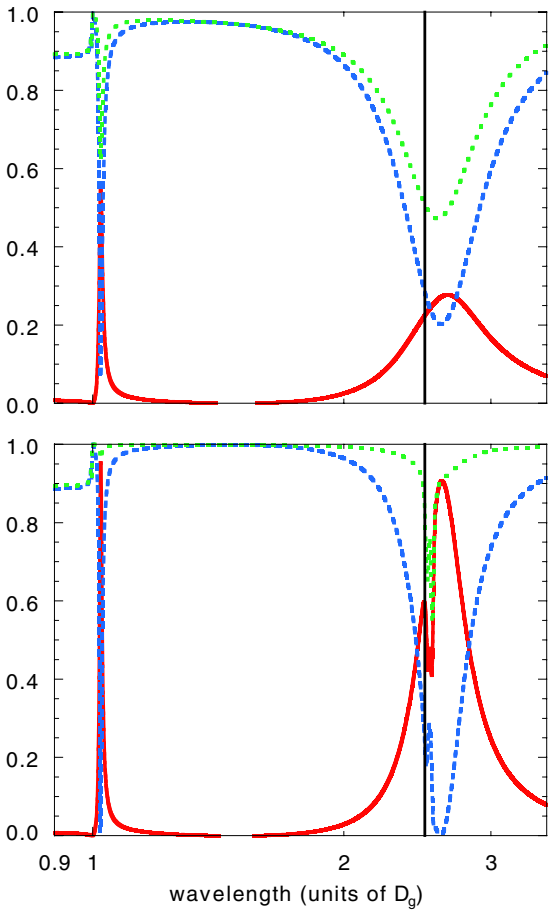

Fig. 9. Calculated zero-order reflection (red curves) and transmission (dashed-blue curves) coefficients for the ionic crystal grating. The sum of the reflection and transmission coefficients is shown as the dashed-dotted green curve. The geometry of the grating structure is set by $D_T/D_g = 2.5$. The upper panel of the figure corresponds to the attenuation $\eta = 11.51$ meV. The lower panel of the figure corresponds to the attenuation reduced by a factor of 20: $\eta \to \eta/20$. The vertical black line defines the resonant wavelength $\lambda = D_T = 2\pi c/\omega_T$. (For interpretation of the references to color in this figure legend, the reader is referred to the web version of this article.)

$\varepsilon = \varepsilon_0$ is turned into the polaritonic resonance and follows the diagonal of the plot ($\lambda/D_g = D_T/D_g$). At the same time, starting approximately with $D_T/D_g = 2$, the "narrow" structure resonance associated with $\varepsilon = \varepsilon_\infty$ emerges and fully develops for $D_T/D_g = 4$.

Finally, we would like to show the sensitivity of the results to the attenuation in the present system. In Fig. 9, the transmission and reflection coefficients are presented for two different choices of the attenuation η in (3.6). The geometry of the grating structure is set by $D_T/D_g = 2.5$. The upper panel of the figure corresponds to $\eta = 11.51$ meV as used in the calculations above. The lower panel of the figure corresponds to the attenuation reduced by the factor of 20: $\eta \to \eta/20$. Overall features are qualitatively the same in both cases. Thus, both the structure resonance at $\lambda \sim D_g$ and polaritonic resonance at $\lambda \sim 2.5D_g$ are present, accompanied by the reduced transmission and enhanced reflection. As the wavelength increases from the structure resonance, the reflectivity of the grating drops to zero. Its subsequent onset for $\lambda > 1.683D_g$ is linked with the metallic-type behavior of the ionic crystal (ε becomes negative). The characteristic frequency for "metallization" can be deduced from the Lyddane–Sachs–Teller relation $\omega_L = \omega_T\sqrt{\varepsilon_0/\varepsilon_\infty}$, leading to $\lambda_L = 1.683D_g$ for $\lambda_T = 2.5D_g$. Despite these common features, the reduction of the attenuation leads to essential changes. In contrast to the upper panel of the figure, for $\eta \to \eta/20$ the transmission coefficient reaches nearly 0 at both the resonances, and the reflection coefficient is close to 1. Moreover, new structures appear in the polaritonic resonance for $\lambda = D_T$, i.e., as ε changes from large negative to large positive values. These structures are completely washed out for the medium with large damping. This result indicates the importance of accurate modeling of losses in polaritonic media in order to make reliable predictions of transmission and reflection properties of grating structures and photonic crystals.

7. Conclusions

It has been demonstrated that the Lanczos algorithm can be used to develop highly efficient, accurate, and unconditionally stable propagation schemes to simulate scattering of broad-band electromagnetic pulses in passive media. The accuracy and efficiency of the algorithm have been illustrated with an example of the electromagnetic wave propagation in vacuum. At the same computational costs, a significant reduction of phase and amplitude errors has been observed in the Lanczos propagation method as compared to the second-order finite-difference (leapfrog) scheme.

As an example of possible applications, the Lanczos propagation method has been applied to study resonant transmission and reflection of various periodic nanostructures: Arrays of periodically placed parallel cylinders made of non-dispersive dielectric materials as well as ionic crystal materials, and metallic gratings and grooves. The time-domain study clearly demonstrates the role played by quasi-stationary (trapped) electromagnetic waves supported by the corresponding periodic structure in the extraordinary transmission (reflection) properties of the grating. The results for metallic gratings and grooves coincide with those obtained earlier by means of other numerical algorithms. In the case of ionic crystal gratings, we have shown the significance of both structure (or guided wave) resonances and polaritonic excitations for the transmission and reflection properties of grating structures. The results are also shown to be sensitive to the attenuation of polaritonic media.

In summary, we have developed an unconditionally stable (time-domain) algorithm for initial-value problems in the electrodynamics of inhomogeneous, dispersive, and absorptive media. The method is based on three essential ingredients: (i) the Hamiltonian formalism in electrodynamics of passive media, (ii) the Lanczos propagation scheme, modified to account for attenuation, and (iii) the Fourier pseudospectral method on non-uniform grids induced by change of variables to enhance the sampling efficiency in the vicinity of sharp inhomogeneities of the medium. In addition to unconditional stability, the algorithm allows for a dynamical accuracy control, meaning that the two propagation parameters, the dimension of the Krylov space and the time step, may automatically be adjusted to minimize computational costs in due

course of simulations, while still controlling error. The method is applicable to various electromagnetic systems (no restrictions on the Hamiltonian). It is important to emphasize that all these virtues are hardly available in other unconditionally stable algorithms in numerical electrodynamics of passive media.

Acknowledgments

It is a pleasure for us to acknowledge the financial support and kind hospitality of Donostia International Physics Center (DIPC), San-Sebastian, Spain, in the early stage of this project. S.V.S. thanks the LCAM of the University of Paris-Sud and, in particular, Dr. V. Sidis for the support and warm hospitality extended to him during his stay in Orsay. S.V.S. is also grateful to Dr. R. Albanese (US Air Force Brooks Research Center, TX), Professors J.R. Klauder and T. Olson (University of Florida) for the continued support of this project. We thank Dr. D. Wack (KLA-Tencor, San Jose, CA) for stimulating and supporting the work on this project.

References

[1] E. Yablonovitch, Phys. Rev. Lett. 58 (1987) 2059;
J.D. Joannopoulos, R.D. Meade, J.N. Winn, Photonic crystals, Princeton University Press, Princeton, NJ, 1995;
H.J. Lezec, A. Degiron, E. Devaux, R.A. Linke, L. Martin-Moreno, F.J. Garcia-Vidal, T.W. Ebbesen, Science 297 (2002) 820.
[2] T.W. Ebbesen, H.J. Lezec, H.F. Ghaemi, T. Thio, P.A. Wolff, Nature (London) 391 (1998) 667.
[3] R.E. Wyatt, Z.H. Zhang, Dynamics of Molecules and Chemical Reactions, Marcel Dekker, NY, 1996.
[4] S. Chelkowski, C. Foisy, A.D. Bandrauk, Phys. Rev. A 57 (1998) 1176;
L. Malegat, P. Selles, A.K. Kazansky, Phys. Rev. Lett. 85 (2000) 4450;
C. Lemell, X.-M. Tong, F. Krausz, J. Burgdörfer, Phys. Rev. Lett. 90 (2003) 076403.
[5] For a review of different propagation schemes for the time-dependent Schrödinger equation see: C. Leforestier, R.H. Bisseling, C. Cerjan, M.D. Feit, R. Friesner, A. Guldberg, A. Hammerich, G. Jolicard, W. Karrlein, H.-D. Meyer, N. Lipkin, O. Roncero, R. Kosloff, J. Comput. Phys. 94 (1991) 59 (references therein).
[6] C. Cerjan (Ed.), Numerical Grid Methods and Their Application to Schrödinger's Equation, NATO ASI Series, Series C: Mathematical and Physical Sciences, vol. 412, Kluwer Academic Publishers, London, 1993.
[7] M.R. Wall, D. Neuhauser, J. Chem. Phys. 102 (1995) 8011;
V.A. Mandelshtam, H.S. Taylor, Phys. Rev. Lett. 78 (1997) 3274.
[8] D. Neuhauser, M. Baer, J. Phys. Chem. 94 (1990) 185;
M.-C. Heitz, H.-D. Meyer, J. Chem. Phys. 114 (2001) 1382.
[9] A.J.H.M. Meijer, E.M. Goldfield, S.K. Gray, G.G. Balint-Kurti, Chem. Phys. Lett. 293 (1998) 270.
[10] E. Nelson, J. Math. Phys. 5 (1964) 332.
[11] M.D. Feit, J.A. Fleck Jr., Appl. Opt. 17 (1978) 3990.
[12] S.V. Shabanov, Electromagnetic pulse propagation in passive media by path integral methods, a LANL e-preprint, 2003. Available from: <http://xxx.lanl.gov/abs/math.NA/0312296>.
[13] H. De Raedt, K. Michielsen, J.S. Kole, M.T. Figge, Phys. Rev. E 67 (2003) 056706;
H. De Raedt, K. Michielsen, J.S. Kole, M.T. Figge, IEEE Trans. Antenn. Propag. 51 (2003) 3155.
[14] D. Neuhauser, R. Baer, J. Theor. Comput. Chem. 2 (2003) 537.
[15] C.J. Lanczos, J. Res. Natl. Bur. Stand. 45 (1950) 255.
[16] W.E. Arnoldi, Q. Appl. Math. 9 (1951) 17.
[17] H.A. van der Vorst, Iterative Krylov Methods for Large Linear Systems, Cambridge University Press, Cambridge, 2004.
[18] T.J. Park, J.C. Light, J. Chem. Phys. 85 (1986) 5870.
[19] R.W. Wood, Phys. Rev. 48 (1935) 928.
[20] R. Magnusson, S.S. Wang, Appl. Phys. Lett. 61 (1992) 1022;
S. Peng, G.M. Morris, Opt. Lett. 21 (1996) 549;
T. Peter, R. Bräuer, O. Bryngdahl, Opt. Commun. 139 (1997) 177;
K. Koshino, Phys. Rev. B 67 (2003) 165213;
L. Pilozzi, A. D'Andrea, R. Del Sole, Phys. Rev. B 54 (1996) 10763.
[21] A. Rung, C.G. Ribbing, Phys. Rev. Lett. 92 (2004) 123901.

[22] K.C. Huang, P. Bienstman, J.D. Joannopoulos, K.A. Nelson, S. Fan, Phys. Rev. Lett. 90 (2003) 196402.
[23] D. Kosloff, R. Kosloff, J. Comput. Phys. 52 (1983) 35.
[24] J.P. Boyd, Chebyshev and Fourier Spectral Methods, Springer-Verlag, New York, 1989.
[25] R. Richtmyer, K. Morton, Difference Methods for Initial-value Problems, Willey, NY, 1967.
[26] B.N. Parlett, D.S. Scott, Math. Comput. 33 (1979) 217;
H.D. Simon, Linear Algebra Appl. 61 (1984) 101.
[27] P.M. Goorjian, A. Taflove, Opt. Lett. 17 (1992) 180;
L. Gilles, S.C. Hagness, L. Vázquez, J. Comput. Phys. 161 (2000) 379.
[28] A. Taflove, S.C. Hagness, Computational Electrodynamics: the Finite-difference Time-domain Methoartech House, Artech House, Norwood, MA, 2000.
[29] P.G. Petropoulos, SIAM J. Appl. Math. 60 (2000) 1037;
J.-L. Vay, J. Comput. Phys. 165 (2000) 511.
[30] A.G. Borisov, S.V. Shabanov, J. Comput. Phys. 199 (2004) 742.
[31] K.S. Yee, IEEE Trans. Antenn. Propag. 14 (1966) 302.
[32] E. Gallopoulos, Y. Saad, SIAM J. Sci. Statist. Comput. 13 (1992) 1236;
Y. Saad, SIAM J. Numer. Anal. 29 (1992) 209.
[33] M. Hochbruck, C. Lubich, SIAM J. Numer. Anal. 34 (1997) 1911.
[34] T.-W. Lee, S.C. Hagness, J. Opt. Soc. Am. B 21 (2004) 330.
[35] F.J. Garcia-Vidal, L. Martin-Moreno, Phys. Rev. B 66 (2002) 155412.
[36] U. Schröter, D. Heitmann, Phys. Rev. B 58 (1998) 15419;
J.A. Porto, F.J. Garcia-Vidal, J.B. Pendry, Phys. Rev. Lett. 83 (1999) 2845;
Y. Takakura, Phys. Rev. Lett. 86 (2001) 5601;
M.M.J. Treacy, Appl. Phys. Lett. 75 (1999) 606;
M.M.J. Treacy, Phys. Rev. B 66 (2002) 195105;
Q. Cao, Ph. Lalanne, Phys. Rev. Lett. 88 (2002) 057403;
P. Lalanne, C. Sauvan, J.P. Hugonin, J.C. Rodier, P. Chavel, Phys. Rev. B 68 (2003) 125404;
J.M. Steele, C.E. Moran, A. Lee, C.M. Aguirre, N.J. Halas, Phys. Rev. B 68 (2003) 205103;
S.A. Darmanyan, A.V. Zayats, Phys. Rev. B 67 (2003) 035424;
F. Yang, J.R. Sambles, Phys. Rev. Lett. 89 (2002) 063901;
W.-C. Tan, T.W. Preist, R.J. Sambles, Phys. Rev. B 62 (2000) 11134.
[37] F.J. Garcia-Vidal, H.J. Lezec, T.W. Ebbesen, L. Martin-Moreno, Phys. Rev. Lett. 90 (2003) 213901;
P. Kramper, M. Agio, C.M. Soukoulis, A. Birner, F. Müller, R.B. Wehrspohn, U. Gösele, V. Sandoghdar, Phys. Rev. Lett. 92 (2004) 113903;
K.J. Klein Koerkamp, S. Enoch, F.B. Segerink, N.F. van Hulst, L. Kuipers, Phys. Rev. Lett. 92 (2004) 183901.
[38] J. Sjakste, A.G. Borisov, J.P. Gauyacq, A.K. Kazansky, J. Phys. B: At. Mol. Phys. 37 (2004) 1593.
[39] L.-S. Chen, C.-H. Kuo, Z. Ye, Phys. Rev. E 69 (2004) 066612;
E. Chow, S.Y. Lin, S.G. Johnson, P.R. Villeneuve, J.D. Joannopoulos, J.R. Wendt, G.A. Vawter, W. Zubrzycki, H. Hou, A. Alleman, Nature 407 (2000) 983.